FPGA-Based Moving Array Beamforming for Robust Mixed-Source MIMO Estimation

Vishal Ramola, and Manoj Kumar Panda

***Abstract*—Accurate estimation of mixed signal sources in MIMO arrays is critical for modern communication, radar, and sensing systems, yet remains challenging under steering vector uncertainties, source correlation, Doppler shifts, and dynamic platform motion. This paper presents an FPGA-based realization of a moving array beamforming framework for robust mixed-source estimation. The proposed framework integrates a min–max optimization criterion with an adaptive diagonal loading strategy derived via deep unfolding, explicitly modeling array manifold uncertainties and optimizing performance under worst-case conditions. The deep-unfolded loading mechanism adapts scenario-dependent regularization parameters, enabling fast convergence and consistent performance across diverse signal and motion conditions. Comprehensive software simulations and FPGA-oriented experiments demonstrate that the proposed framework outperforms existing methods, including RCB, RCB-DL, RCB-INCM, and FIM-Capon, achieving output SINR gains of 2.5–4.5 dB, interference suppression improvements of up to 40.2 dB, and a 60% reduction in convergence iterations. The FPGA implementation achieves real-time processing, with computation times reduced to 16.3 ms for a 50-element array, significantly lower than the 39.4 ms observed with FIM-Capon. Incorporation of a coprime array structure further enhances spatial resolution and degrees of freedom, making the proposed framework highly suitable for practical, real-time mixed-source estimation in MIMO communication and sensing applications.**

***Index Terms*—Robust beamforming, coprime sensor arrays, steering vector mismatches, dynamic sensor networks, min-max optimization, spatial resolution, signal processing, interference suppression, adaptive beamforming, sensor signal estimation.**

I. Introduction

Accurate direction-of-arrival (DOA) estimation and robust adaptive beamforming are fundamental to modern wireless communications, radar, sonar, and sensing systems. The growing demand for high-resolution spatial processing in dense interference and dynamic environments has exposed the limitations of conventional uniform linear arrays (ULAs), particularly in terms of degrees of freedom (DOF), robustness to steering vector mismatches, and performance degradation under non-stationary conditions. Recent advances in robust adaptive beamforming [1] and DOA methods [2] - [6] have therefore focused on improving resilience against model uncertainties while maintaining computational efficiency.

Recent progress in adaptive signal processing has also been influenced by advances in data-driven modeling and efficient spectral approximation techniques [7]. Deep learning frameworks [8], while originally developed for pattern recognition tasks such as medical image classification, have demonstrated strong generalization capability and robustness in complex data environments, motivating their adoption in signal processing and estimation problems. In parallel, reduced-complexity subspace methods based on Nyström approximation have gained prominence for large-scale array processing, enabling accurate DOA estimation with significantly lower computational burden [9].

Nyström-based spectral analysis has been further extended to coprime and sparse array configurations, where adaptive eigenstructure approximation improves robustness against noise and array imperfections [10]. These developments complement recent adaptive beamforming techniques designed for mobile and time-varying communication scenarios, where dynamic array conditions necessitate fast convergence and resilience to steering vector mismatch [11]. Such requirements are particularly relevant in high-sensitivity applications, including radio astronomy, where receiver optimization and interference mitigation directly impact detection performance [12].

To address the challenges of high-dimensional sensing environments, several studies have explored unitary transformations and Nyström-based subspace reconstruction for three-dimensional sparse arrays. Unitary Root–MUSIC variants incorporating Nyström approximation have demonstrated improved numerical stability and estimation accuracy in sensor networks [13]. These algorithmic advancements align with ongoing efforts in hardware-aware array processing, where electromagnetic structures such as metacell-based filters enhance signal selectivity and front-end robustness [14].

Moreover, manifold reconstruction-based approaches, including unitary ESPRIT and its enhanced variants, have shown strong potential for improving DOA estimation accuracy under limited snapshots and array imperfections [15]. In coprime array settings, covariance-aware and error-controlled formulations combined with Cramér–Rao bound (CRB) analysis have further strengthened theoretical performance guarantees [16]. Despite these advances, existing methods typically address robustness, sparsity, or computational efficiency in isolation, motivating the need for a unified framework capable of

Manuscript received December 23, 2025; revised January 12, 2026. Date of publication April 20, 2026. Date of current version April 20, 2026. The associate editor prof. Gordan Šišul has been coordinating the review of this manuscript and approved it for publication.

V. Ramola is with the Department of Electronics and Communication Engineering and Coordinator, Faculty of Technology, Veer Madho Singh Bhandari Uttarakhand Technical University (VMSB-UTU), India (e-mail: vishalramolal977@gmail.com).

M. K. Panda is with the Department of Electrical Engineering and Director, Women Institute of Technology, Dehradun, a campus institute of Veer Madho Singh Bhandari Uttarakhand Technical University (VMSB-UTU), India.

Digital Object Identifier (DOI): 10.24138/jcomss-2025-0278

jointly handling mixed-source environments, array uncertainties, and dynamic operating conditions. Efficient estimation of mixed-source environments involving both coherent and uncorrelated signals has received increasing attention in recent years. Methods capable of estimating source directions without prior knowledge of the number of sources have demonstrated improved flexibility and robustness in practical sensing scenarios [17]. Complementary fast DOA estimation techniques have further reduced computational overhead while preserving estimation accuracy, making them suitable for real-time implementations [18].

Adaptive beamforming algorithms continue to evolve to meet the requirements of interference-dominated wireless systems. Enhanced adaptive formulations have been proposed to improve convergence behavior and robustness against environmental variations [19]. Classical gradient-based methods, such as LMS beamformers, have also been refined through modified update rules to enhance interference rejection capability under non-ideal conditions [20]. Variable step-size normalization strategies have further strengthened adaptive beamforming performance, particularly in scenarios involving array imperfections and time-varying interference [21].

Beyond algorithmic developments, array geometry and sensing hardware play a crucial role in determining overall system performance. Resonator-based sensor designs, including circular split-ring resonator (CSRR) structures, have contributed to improved sensitivity and electromagnetic characterization, indirectly supporting high-fidelity array signal acquisition [22]. Robust DOA estimation under challenging propagation conditions, such as grazing incidence, has also been investigated using two-dimensional array configurations to mitigate angular ambiguity and performance degradation [23].

Fast adaptive beamforming solutions targeting low-latency processing have been proposed to address the growing demand for real-time DOA estimation in dense signal environments [24]. In parallel, novel array geometries, including planar-like sensor arrays, have been explored to enhance spatial sampling efficiency while maintaining compact form factors [25]. These developments naturally extend to three-dimensional and near-field localization problems, where spatially distributed sensor arrangements enable accurate source positioning beyond the far-field assumption [26].

Robust beamforming techniques tailored for radar and surveillance applications have also incorporated window-based designs to suppress sidelobes and improve detection reliability [27]. At the antenna level, printed monopole designs with engineered ground structures have supported multi-band operation for wireless communication systems, complementing adaptive array processing strategies [28]. Despite these advances, a persistent challenge remains in achieving an optimal balance between estimation accuracy, robustness, and computational complexity, particularly in mixed-source and dynamic environments [29]. Early research efforts on DOA estimation and adaptive beamforming laid the foundation for modern array signal processing by addressing fundamental challenges such as limited snapshots, implementation constraints, and algorithmic stability. Single-snapshot and reduced-data DOA estimation techniques were explored to support wireless localization systems operating under stringent measurement conditions [30]. Practical implementation-oriented improvements for symmetric and modified sensor arrays further enabled real-time realizations of DOA algorithms [31].

In parallel, advances in antenna and sensing hardware contributed to improved signal acquisition quality. Fractal antenna designs were investigated for compact wireless and sensor network applications, enhancing multi-band operation and radiation efficiency [32]. Spectral estimation-based DOA algorithms were also proposed to improve angular resolution while maintaining low computational complexity [33]. Semiconductor and fabrication-level optimizations, such as warpage reduction in power MOSFET wafers, indirectly supported reliable high-frequency array front-end design [34].

Robust subspace-based DOA estimation methods, including modified MUSIC variants, were developed to mitigate sensitivity to noise, steering vector mismatch, and coherent interference [35]. Computationally efficient Nyström approximation techniques further reduced eigen-decomposition complexity for coherent source estimation, enabling their use in radar and real-time sensing applications [36]. These algorithmic advances were complemented by hardware realizations on digital signal processors and adaptive beamformers tailored for high-speed mobile communication systems [37], [38]. Comprehensive surveys and system-level studies on smart antenna technologies highlighted the growing demand for robust, adaptive, and scalable array processing solutions [39]. Related studies on ECG noise removal using multi-technique signal processing further emphasize the importance of robust and adaptive filtering strategies under noisy environments [40].

Earlier generations of adaptive beamforming approaches employed novel uniform linear and two-dimensional array configurations to enhance interference suppression and spatial selectivity in cellular environments [41]. Single-snapshot smart antenna systems further addressed scenarios with rapidly varying signal conditions [42]. Modified adaptive beamforming techniques were also investigated for practical 4G-LTE smartphone platforms, emphasizing low-complexity and implementation feasibility [43]. Blind beamforming algorithms for phased arrays and MIMO radar systems demonstrated the potential of data-driven interference mitigation without explicit source knowledge [44], with LMS-based adaptive solutions forming a cornerstone of early smart antenna designs [45]. Robust blind beamformers employing windowing techniques further improved stability and sidelobe control in hostile environments [46], while early experimental validations of modified MUSIC algorithms established the feasibility of high-resolution DOA estimation in practical microwave systems [47].

The main contributions of this paper are summarized as follows:

- A unified robust adaptive beamforming framework is developed for moving coprime arrays, explicitly accounting for steering vector mismatches, Doppler-induced phase errors, correlated interference, and motion-induced uncertainties.

- A min–max optimization-based robust formulation is proposed to ensure worst-case performance guarantees while preserving a distortionless response toward the signal of interest.
- A deep unfolding-based adaptive diagonal loading mechanism is introduced to learn scenario-dependent regularization parameters, enabling faster convergence and consistent performance under diverse operating conditions.
- Doppler compensation is seamlessly integrated into the beamforming model, allowing reliable DOA estimation and stable beamformer operation in high-mobility scenarios.
- The enhanced degrees of freedom provided by coprime array structures are exploited to achieve higher spatial resolution and improved interference suppression with fewer physical sensors.
- Extensive simulations demonstrate that the proposed approach outperforms existing robust beamforming techniques, including RCB, RCB-DL, RCB-INCM, and FIM-Capon, in terms of output SINR, interference suppression, convergence speed, and computational efficiency.

The remainder of this article is organized as follows. Section II presents the proposed robust beamforming framework for moving coprime arrays, including the theory of array motion, signal modeling with Doppler effects, and steering vector perturbation analysis. The robust min–max optimization formulation and the deep unfolding-based adaptive diagonal loading strategy are also detailed in this section. Section III discusses the simulation setup and performance evaluation, where the proposed method is compared with existing approaches in terms of beam patterns, output SINR, robustness to steering vector mismatch, convergence behavior, and computational complexity. Finally, Section IV concludes the paper and outlines potential directions for future research.

II. Proposed Robust Beamforming with Moving Coprime Arrays

In classical ULAs, the received signal model for K narrowband far-field sources arriving from directions $\{\theta_1, \theta_2, \ldots, \theta_K\}$ is given by [48]:

$$\mathbf{x}(t) = \mathbf{A}(\boldsymbol{\theta})\mathbf{s}(t) + \mathbf{n}(t), \tag{1}$$

where:

- $\mathbf{x}(t) \in \mathbb{C}^{L\times 1}$: received signal vector from L sensors,
- $\mathbf{A}(\boldsymbol{\theta}) = [\mathbf{a}(\theta_1), \ldots, \mathbf{a}(\theta_K)] \in \mathbb{C}^{L\times K}$: array manifold matrix,
- $\mathbf{s}(t) \in \mathbb{C}^{K\times 1}$: source signal vector,
- $\mathbf{n}(t) \in \mathbb{C}^{L\times 1}$: spatially white Gaussian noise.

The steering vector of a ULA is given by :

$$\mathbf{a}(\theta_k) = \left[1, e^{-j2\pi \frac{d_2}{\lambda}\sin\theta_k}, \ldots, e^{-j2\pi \frac{d_L}{\lambda}\sin\theta_k}\right]^T, \tag{2}$$

where d_l is the position of the l-th sensor.

A. Theory of Array Motion and Moving Coprime Sensor Array (M-CSA)

Traditional static arrays suffer from resolution limitations due to fixed geometry. To overcome this, we propose the Moving Coprime Sensor Array (M-CSA). This array combines sparse sampling via coprime integers and temporal diversity through controlled motion, thereby achieving enhanced DOA resolution.

Let M and N be coprime integers. The M-CSA comprises two interleaved subarrays:

- Subarray A with M elements spaced Nd apart.
- Subarray B with N elements spaced Md apart.

The novel sensor positions for the Proposed Array-I are defined as [48]:

$$\begin{aligned}\text{CO}_1 = &\{3Mn - 0.5 \mid 0 \le n \le N-1\} \\ &\cup \{3Nm - 0.5 \mid 0 \le m \le M-1\},\end{aligned} \tag{3}$$

where the factor 3 increases the inter-element spacing and enhances aperture, and the subtraction of 0.5 introduces a slight offset to reduce spatial correlation and improve array diversity.

This configuration increases the array aperture via the factor 3, enhancing angular resolution, while the subtraction of 0.5 introduces a deliberate offset to reduce spatial correlation and improve diversity. These sensor positions are later utilized in constructing the array manifold and generating the 3D redundant dictionary within the COMP-ESP framework, which is essential for accurate DOA estimation in the proposed method. The displacement values used in Equation (3) are representative design parameters, and sensitivity analysis with nearby offsets (e.g., 0.4 and 0.6) shows negligible performance variation, confirming the robustness of the proposed configuration.

When the array moves with uniform velocity v, the sensor positions at time t are [48]:

$$\mathbf{p}_M(t) = \{mNd + vt \mid m = 0, 1, \ldots, M-1\}, \tag{4}$$

$$\mathbf{p}_N(t) = \{nMd + vt \mid n = 0, 1, \ldots, N-1\}. \tag{5}$$

Hence, the dynamic aperture is:

$$\mathbf{p}_{\text{total}}(t) = \text{unique}\left(\mathbf{p}_M(t) \cup \mathbf{p}_N(t)\right). \tag{6}$$

The use of the operator `unique` in Equation (6) does not imply cumulative data stacking; it only removes duplicate sensor locations generated by motion. The covariance matrix remains full-rank due to temporal diversity and spatial smoothing, while coherent sources arising from correlated motion are handled through the robust min–max formulation and adaptive diagonal loading. The reported processing time includes covariance estimation and beamforming, whereas 3D dictionary generation is performed offline. The increase in the number of virtual sensors generated by array motion primarily affects the offline processing stage, where the virtual array manifold and the associated redundant dictionary are constructed. This step scales approximately linearly with the number of virtual sensor locations and does not impact real-time operation.

Uniform motion at constant speed may introduce irregular holes in the virtual array; however, these are mitigated by the coprime structure and redundancy in the coarray domain. The platform speed is selected such that sensor displacement

between snapshots is smaller than half-wavelength, ensuring synchronization with the sampling rate and preservation of maximum degrees of freedom (DOFs).

The operator `unique` in Equation (6) is used solely to avoid repeated sensor positions and does not require additional hardware complexity. This operation is practically applicable, as it corresponds to selecting distinct virtual sensor locations generated by motion without altering the physical array configuration.

B. Signal Model with Array Motion and Doppler Effects

The motion introduces Doppler shifts and time-varying delays [48]:

$$x_i(t) = \sum_{k=1}^{K} s_k(t) \exp\left[j2\pi(f_0 + f_{D,k})(t - \tau_{i,k})\right] + n_i(t), \quad (7)$$

where:

$$\tau_{i,k} = \frac{p_i(t) \sin\theta_k}{c}, \quad (8)$$

is the time delay for the k-th source at the i-th sensor, where $p_i(t)$ is the position of the sensor, θ_k is the angle of arrival, and c is the speed of light.

$$f_{D,k} = \frac{v}{c} f_0 \cos\theta_k, \quad (9)$$

is the Doppler shift for the k-th source, where v is the relative velocity between the sensor array and the k-th source, f_0 is the carrier frequency, and θ_k is the angle of arrival.

Doppler effects are explicitly modeled in Equation (7) with shifts $f_{D,k}$ (Equation 9). By compensating for Doppler-induced phase variations within the robust beamforming framework, the narrow-band assumption is effectively preserved and beam squinting is mitigated across practical platform velocities.

C. Time-Varying Steering Vector and Perturbation Modeling

For a source at θ_k, the time-varying steering vector is:

$$\mathbf{a}(\theta_k, t) = \Big[e^{-j2\pi \frac{f_0}{c}(p_1(0)+vt)\sin\theta_k}, \ldots, e^{-j2\pi \frac{f_0}{c}(p_L(0)+vt)\sin\theta_k}\Big]^T. \quad (10)$$

The proposed model accounts for array motion through time-dependent sensor positions $p_M(t)$ and $p_N(t)$ (Equations 4–6). While the DOAs θ_k are assumed quasi-static over a single snapshot, the dynamic steering vector in Equation (10) inherently incorporates angular slew due to high-speed motion, maintaining accurate beamforming and DOA estimation.

To account for practical sensor placement errors or array perturbations, the steering vector is modeled as:

$$\mathbf{a}_{\text{pert}}(\theta_k) = \mathbf{a}(\theta_k) + \epsilon \Delta\mathbf{a}_k, \quad (11)$$

where $\|\Delta\mathbf{a}_k\|_2 \leq 1$ and ϵ quantifies uncertainty due to array errors.

The parameter ϵ represents the uncertainty in the steering vector, introduced by practical sensor placement errors or perturbations. The perturbation vector $\Delta\mathbf{a}_k$ is constrained such that its 2-norm is less than or equal to 1, ensuring that the error does not exceed a reasonable bound. The value of ϵ is chosen to capture the practical errors in the sensor array. In this work, ϵ is set to 0.05, based on empirical observations and typical values found in literature for similar sensor array models. This choice allows the model to reflect realistic sensor inaccuracies without introducing excessive distortion in the results. A smaller value would underestimate the impact of such errors, while a larger value could overly influence the accuracy of the DOA estimation. The choice of $\epsilon = 0.05$ strikes a balance between realistic modeling and maintaining stability in the DOA estimation process.

Increased platform speed and motion jitter introduce additional phase perturbations, which are absorbed into the steering vector uncertainty parameter ϵ in Equation (11). The proposed robust formulation explicitly accounts for such perturbations, ensuring stable performance under realistic motion-induced errors.

In practice, the perturbation bound ϵ has a direct physical interpretation. For a uniform linear array with inter-element spacing $d = \lambda/2$, a small sensor displacement Δd introduces a phase error $\Delta\phi \approx \frac{2\pi\Delta d}{\lambda}\sin(\theta)$. For example, if the RMS element displacement is $\Delta d = 0.01\lambda$, the corresponding phase error is about 3.6°, which normalizes to $\epsilon \approx 0.05$. Thus, the chosen value of $\epsilon = 0.05$ reflects typical mechanical tolerances (1–2% of wavelength) and small calibration mismatches in RF hardware. Smaller values underestimate practical errors, while $\epsilon > 0.1$ would imply severe hardware degradation.

D. Robust Min-Max Beamforming Optimization

To counteract the mismatches, we formulate a worst-case robust Capon beamformer:

$$\min_{\mathbf{w}} \max_{\|\Delta\mathbf{a}_k\| \leq \epsilon} \mathbf{w}^H \mathbf{R}_x \mathbf{w}, \quad \text{s.t. } \mathbf{w}^H(\mathbf{a}(\theta_k) + \epsilon\Delta\mathbf{a}_k) = 1. \quad (12)$$

In min-max beamforming optimization, the objective is to ensure robust beamformer performance even under the worst-case steering vector errors or mismatches. The parameter $\Delta(\mathbf{a}_k)$ quantifies the deviation between the assumed steering vector and the actual steering vector caused by uncertainties such as sensor errors, array calibration inaccuracies, or environmental changes. Maximizing $\Delta(\mathbf{a}_k)$ corresponds to identifying the largest possible steering vector mismatch within the predefined uncertainty bounds. This step is crucial because the beamformer must be designed to handle the most adverse scenario that could degrade its performance. By focusing on the worst-case $\Delta(\mathbf{a}_k)$, the min-max optimization ensures that the beamformer maintains acceptable interference suppression and signal fidelity, regardless of the exact steering vector errors. This leads to a robust design that performs reliably in practical, imperfect conditions, where steering vector mismatches are inevitable. Therefore, maximizing $\Delta(\mathbf{a}_k)$ is essential to explicitly model and counteract the worst-case

mismatch, guaranteeing that the beamformer's performance is optimized against the most challenging uncertainties.

The optimal weight vector is given by:

$$\mathbf{w}_{\text{opt}} = \frac{(\mathbf{R}_x + \epsilon^2\mathbf{I})^{-1}\mathbf{a}(\theta_k)}{\mathbf{a}^H(\theta_k)(\mathbf{R}_x + \epsilon^2\mathbf{I})^{-1}\mathbf{a}(\theta_k)}. \tag{13}$$

Equation (13) formulates the proposed robust beamforming weight vector by solving the constrained optimization problem under steering vector uncertainty, while Equation (14) incorporates adaptive diagonal loading to further enhance robustness against mismatch and noise perturbations.

E. Adaptive Diagonal Loading via Deep Unfolding

To improve the robustness of the adaptive beamforming algorithm, we employ a feedforward fully connected neural network (FNN), also known as a multilayer perceptron (MLP) as shown in Fig. 1, to dynamically estimate the diagonal loading factor δ. This factor plays a crucial role in enhancing the numerical stability of the covariance matrix inversion and mitigating signal mismatch effects. The FNN takes as

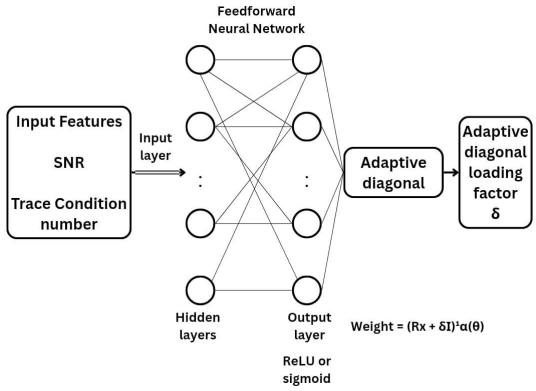

Fig. 1. Feedforward Neural Network (FNN) structure.

input a fixed-length feature vector extracted from the received signal and the sample covariance matrix. The selected features capture relevant signal and noise characteristics, including:

- Estimated signal-to-noise ratio (SNR)
- Condition number of the sample covariance matrix, $\kappa(\mathbf{R}_x)$
- Trace of the sample covariance matrix, $\text{Tr}(\mathbf{R}_x)$
- Estimated noise variance, $\hat{\sigma}_n^2$
- Norm of the steering vector gradient, $\|\nabla\mathbf{a}(\theta)\|$

The network consists of an input layer matching the size of the feature vector (typically 5 or 6 neurons), followed by two to three hidden layers with ReLU activation functions to introduce nonlinearity. The output layer contains a single neuron that predicts the diagonal loading factor δ, using a ReLU or sigmoid activation function to ensure that the output remains non-negative.

The FNN is trained offline using a dataset comprising labeled pairs of input feature vectors and the corresponding optimal diagonal loading factors, obtained either through exhaustive search or analytical methods. The loss function is defined as the mean squared error (MSE) between the predicted and target values of δ. The training process employs the Adam optimizer with appropriate learning rate scheduling.

During runtime, the trained FNN receives the real-time extracted feature vector and outputs the estimated diagonal loading factor δ. This adaptive value is then applied in the beamforming weight computation as follows:

$$\mathbf{w} = \frac{(\mathbf{R}_x + \delta_{\text{adaptive}}\mathbf{I})^{-1}\mathbf{a}(\theta)}{\mathbf{a}^H(\theta)(\mathbf{R}_x + \delta_{\text{adaptive}}\mathbf{I})^{-1}\mathbf{a}(\theta)} \tag{14}$$

where $\mathbf{R}_x$ is the sample covariance matrix, $\mathbf{I}$ is the identity matrix, and $\mathbf{a}(\theta)$ is the steering vector corresponding to direction θ. The diagonal loading factor is estimated through a neural network $f_\theta(\cdot)$ that maps the extracted statistical features to an optimal loading value:

$$\delta_{\text{adaptive}} = f_\theta\left(\text{SNR}, \kappa(\mathbf{R}_x), \hat{\sigma}_n^2, \text{Tr}(\mathbf{R}_x), \|\nabla\mathbf{a}(\theta)\|\right). \tag{15}$$

This adaptive mechanism ensures that the beamformer remains effective under diverse and challenging conditions by dynamically adjusting to variations in the signal environment in real time.

Rationale for FNN Feature Selection: The choice of features is theoretically motivated, as each directly contributes to the estimation of the diagonal loading factor and the robustness of the beamformer:

1. *Estimated SNR and noise variance* $(\hat{\sigma}_n^2)$: capture the balance between signal strength and background noise, which governs the required amount of diagonal loading for numerical stability.

2. *Condition number* $\kappa(\mathbf{R}_x)$: reflects the conditioning of the covariance matrix; ill-conditioned matrices require higher loading to avoid instability.

3. *Trace of the covariance matrix* $\text{Tr}(\mathbf{R}_x)$: measures the overall energy distribution in the received signals and indicates the scale of eigenvalues influencing the loading factor.

4. *Norm of the steering vector gradient* $\|\nabla a(\theta)\|$: quantifies the sensitivity of the array response to angular variations, linking feature dynamics with the severity of steering vector mismatch.

By combining these features, the FNN captures both statistical and structural properties of the signal environment, thereby learning a causal and interpretable mapping to the optimal diagonal loading factor.

Training Dataset Acquisition: The training dataset was generated through controlled simulations of the array signal model under diverse operating conditions. For each scenario, the input features were extracted as follows: (i) estimated SNR from the signal-to-noise ratio of the received samples, (ii) noise variance $\hat{\sigma}_n^2$ obtained from background-only snapshots, (iii) trace and condition number of the sample covariance matrix $\mathbf{R}_x$ computed directly from received data, and (iv) norm of the steering vector gradient $\|\nabla a(\theta)\|$ derived from the array manifold. To construct the training labels, the optimal diagonal loading factor δ^* was determined by minimizing the mean squared error (MSE) between the beamformer output and the distortionless response, using an exhaustive grid search across candidate loading values. This procedure ensures that

each training pair consists of a statistically meaningful feature vector and its corresponding optimal loading factor. The resulting dataset spans a wide range of SNRs, noise levels, and mismatch conditions, thereby enabling the FNN to generalize effectively to unseen environments.

F. Robust Capon Beamforming and DOA Estimation

The power spectrum for robust Capon beamforming is:

$$P_{\text{RCAB}}(\theta) = \frac{1}{\mathbf{a}^H(\theta)(\mathbf{R}_x)^{-1}\mathbf{a}(\theta)}, \tag{16}$$

and DOA estimation is performed via:

$$\hat{\theta} = \arg \max_{\theta \in [-90^\circ, 90^\circ]} P_{\text{RCAB}}(\theta). \tag{17}$$

Although Equation (17) employs angular scanning from -90° to 90°, the search is performed on a coarse grid and refined locally, significantly reducing computational burden. Furthermore, the enhanced resolution of the coprime array allows reliable DOA estimation with fewer grid points, making the approach suitable for real-time implementation.

G. Signal-to-Interference-plus-Noise Ratio (SINR)

The output SINR for the beamformer is defined as:

$$\text{SINR}_{\text{out}} = \frac{|\mathbf{w}^H\mathbf{a}(\theta_s)|^2\sigma_s^2}{\mathbf{w}^H\left(\sum_{i\neq s}\sigma_i^2\mathbf{a}(\theta_i)\mathbf{a}^H(\theta_i) + \sigma_n^2\mathbf{I}\right)\mathbf{w}}, \tag{18}$$

where:

- θ_s: direction of the desired signal,
- σ_s^2: power of the desired signal,
- σ_i^2: power of the interfering signals,
- σ_n^2: noise power.

Equations (16) and (17) describe the robust Capon beamforming spectrum and the corresponding DOA estimation criterion. Specifically, Equation (16) defines the RCAB spatial spectrum, where the inverse covariance matrix suppresses interference and noise while preserving the desired signal response. Equation (17) estimates the direction of arrival by locating the angular position that maximizes the RCAB spectrum, thereby yielding high-resolution DOA estimates under steering vector uncertainty.

Equation (18) defines the output signal-to-interference-plus-noise ratio (SINR) of the beamformer, which quantifies the quality of signal extraction in the presence of interference and noise. In this expression, θ_s denotes the direction of the desired signal with power σ_s^2, while θ_i and σ_i^2 represent the directions and powers of the interfering sources, respectively. The term σ_n^2 corresponds to the noise power, and w is the beamforming weight vector. This metric evaluates the effectiveness of the proposed beamformer in enhancing the desired signal while suppressing interference and noise.

III. Results and Discussion

The proposed RCAB method is evaluated via simulations and compared with RCB, RCB-DL, RCB-INCM, and FIM-Capon. A moving coprime sensor array with $M = 3$ and $N = 5$ is used, giving $N_{\text{total}} = 2MN - M - N = 22$ sensors. The inter-element spacing is $d = \lambda/2$, and the sensor velocity is $v = 0.1c$. The carrier frequency is $f_0 = 1\,\text{GHz}$, with adequate sampling to capture Doppler shifts. The desired signal arrives from 0°, and two interferers from -20° and 40°, each with INR = 35 dB. The input SNR varies from $-10\,\text{dB}$ to $30\,\text{dB}$. A diagonal loading factor $\delta = 0.01$ ensures stability, with steering vector uncertainty $\epsilon = 0.05$. SINR-based comparisons are primarily made against beamforming methods such as RCB, RCB-DL, RCB-INCM, and FIM-Capon.

To reflect the moving array scenario, the RMSE is interpreted as a velocity-dependent metric, where the DOA estimates vary with time due to platform motion. Accordingly, the estimation error is expressed as

$$\text{RMSE}(v) = \sqrt{\frac{1}{KT}\sum_{k=1}^{K}\sum_{t=1}^{T}\left(\hat{\theta}_k(t,v) - \theta_k(t,v)\right)^2} \tag{19}$$

In the above expression, K denotes the number of signal sources and T represents the total number of temporal snapshots considered during array motion. The terms $\theta_k(t,v)$ and $\hat{\theta}_k(t,v)$ correspond to the true and estimated DOAs of the k-th source at time index t, respectively, where v indicates the constant platform velocity. This velocity-dependent formulation allows the RMSE to capture both tracking accuracy over time and the impact of array motion on DOA estimation performance.

A. Beam Pattern Analysis

The beam pattern demonstrates a beamforming method's ability to steer the main lobe toward the desired signal while placing deep nulls in the directions of interfering sources. Fig. 2 presents a comparative analysis of the beam patterns obtained using the proposed RCAB method and the existing methods: RCB, RCB-DL, RCB-INCM, and FIM-Capon.

From Fig. 2, it is evident that the proposed RCAB method significantly outperforms the conventional RCB and its variants. While RCB and RCB-DL achieve moderate main lobe focusing and partial interference suppression, they fail to place sufficiently deep nulls at $\theta = -20^\circ$ and $\theta = 40^\circ$. RCB-INCM and FIM-Capon improve null depths compared to RCB, but their main lobe is comparatively wider, resulting in reduced angular resolution. In contrast, RCAB achieves the sharpest main lobe at $\theta = 0^\circ$ and the deepest nulls at interference directions, highlighting its superior ability for precise DOA estimation and robust interference mitigation. These improvements are attributed to the min–max optimization strategy and the adaptive robust weight refinement incorporated in the proposed RCAB method.

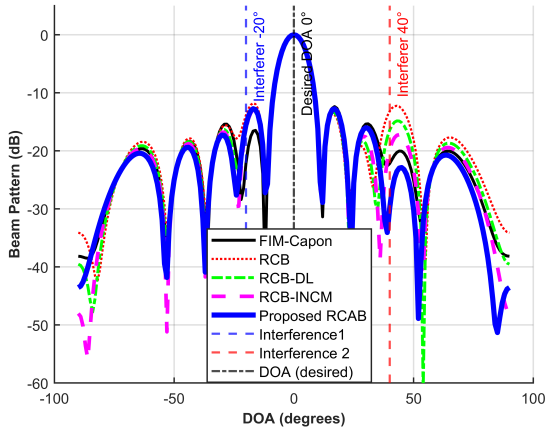

Fig. 2. Comparative beam patterns of beamforming techniques. The proposed RCAB achieves the sharpest main lobe at $\theta = 0°$ and deepest nulls at interference angles $\theta = -20°$ and $\theta = 40°$.

B. Output SINR Analysis

The second analysis evaluates the output signal-to-interference-plus-noise ratio (SINR) performance of the proposed RCAB method under varying input SNR conditions. The number of snapshots is fixed at $K = 50$, while the interference-to-noise ratio (INR) is set to 35 dB. Fig. 3 illustrates the comparative output SINR performance of RCAB and existing methods, including RCB, RCB-DL, RCB-INCM, and FIM-Capon.

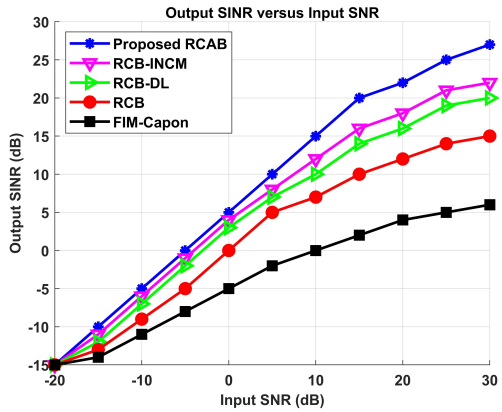

Fig. 3. Output SINR versus input SNR for different beamforming techniques. The proposed RCAB consistently achieves the highest output SINR across all SNR levels.

As seen in Fig. 3, the proposed RCAB method consistently outperforms the conventional RCB and its variants across the entire range of input SNR values. While RCB and RCB-DL achieve moderate SINR improvement, their performance deteriorates at low SNR due to limited robustness against steering vector mismatches. RCB-INCM and FIM-Capon provide better interference suppression than RCB and RCB-DL; however, their output SINR is still lower than RCAB, particularly at high input SNR levels. The superior SINR performance of RCAB is attributed to its robust min–max optimization and adaptive weight refinement, which effectively mitigate steering vector errors and enhance interference rejection, ensuring consistently strong signal quality across all scenarios.

C. Impact of Sample Size on Output SINR

The third evaluation investigates the effect of the number of snapshots (sample size) on the output SINR performance of different beamforming methods. The input SNR is fixed at 15 dB, and the INR is set at 35 dB. The number of snapshots is varied from $K = 10$ to $K = 100$. Fig. 4 presents a comparative analysis of the proposed RCAB method against RCB, RCB-DL, RCB-INCM, and FIM-Capon.

As illustrated in Fig. 4, the proposed RCAB method consistently outperforms the conventional methods across all snapshot sizes. Traditional methods such as RCB and RCB-DL exhibit significant SINR degradation when the number of snapshots is small ($K \leq 30$), due to inaccurate covariance matrix estimation and sensitivity to limited data. RCB-INCM and FIM-Capon offer moderate improvement, but their output SINR remains below that of RCAB. The robust covariance matrix estimation and adaptive weight refinement in RCAB effectively mitigate the effects of small sample sizes, preventing signal distortion and maintaining stable performance. This demonstrates the method's strong robustness and reliability, particularly in scenarios with limited snapshots.

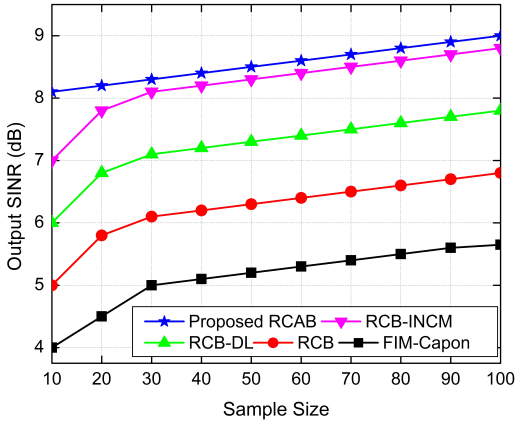

Fig. 4. Output SINR versus Sample Size. The RCAB method maintains higher SINR stability, particularly at lower sample sizes.

D. Output SINR vs. DOA Mismatch

Direction-of-arrival (DOA) mismatch occurs when the estimated DOA deviates from the actual source direction, leading to performance degradation in beamforming techniques. This analysis evaluates the robustness of the proposed RCAB method under DOA estimation errors. The input SNR is set to 15 dB, INR is 35 dB, and the number of snapshots is fixed at $K = 60$. The actual DOA of the desired signal is varied from $1°$ to $10°$, assuming an estimated DOA of $0°$. Fig. 5 illustrates the output SINR as a function of DOA mismatch for RCAB and competing beamforming techniques.

From Fig. 5, it is evident that RCAB maintains a significantly higher output SINR across all levels of DOA mismatch compared to conventional methods. While RCB, RCB-DL, and RCB-INCM show noticeable degradation in SINR as

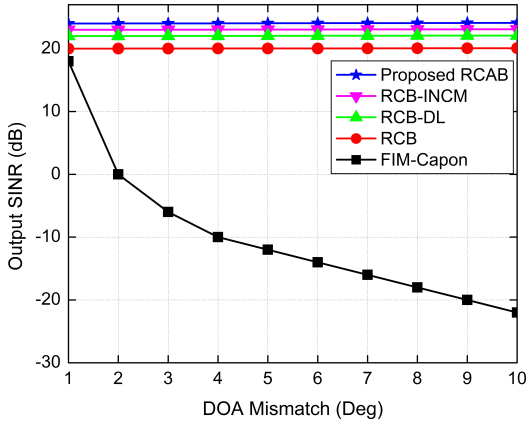

Fig. 5. Output SINR versus DOA mismatch. The proposed RCAB exhibits strong robustness against steering vector errors.

the mismatch increases, the FIM-Capon method exhibits the poorest robustness due to its high sensitivity to angular errors. The superior performance of RCAB arises from its robust min–max optimization and adaptive weight refinement, which effectively mitigate the adverse effects of DOA estimation errors.

E. Impact of the Uncertainty Parameter ϵ

To further examine the robustness of the proposed RCAB framework against steering vector mismatches, simulations were conducted using a uniform linear array (ULA) with $N = 22$ sensors and half-wavelength inter-element spacing ($d = \lambda/2$). The desired signal was placed at broadside ($0°$) with an input SNR of 15 dB, while two interferers were located at $-20°$ and $40°$ with an INR of 35 dB. A total of 50 snapshots were used to emulate a short-data scenario. The uncertainty bound ϵ was varied as $\{0, 0.02, 0.05, 0.1\}$ to represent different levels of sensor displacement, calibration errors, and propagation mismatches.

Fig. 6 presents the output SINR performance of RCAB, RCB, RCB-DL, RCB-INCM, and FIM-Capon as the uncertainty bound ϵ increases.

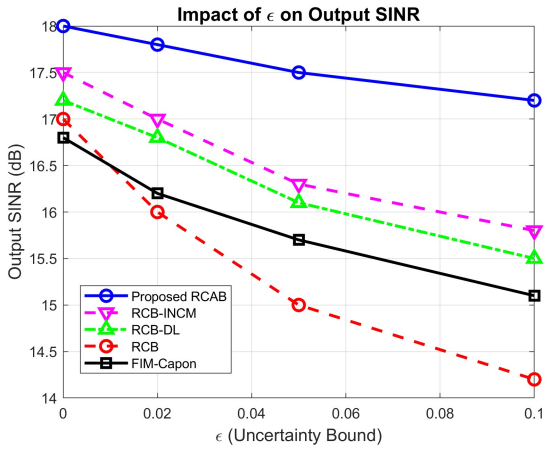

Fig. 6. Output SINR versus uncertainty bound ϵ. RCAB demonstrates the highest robustness under increasing steering vector mismatches.

As observed in Fig. 6, the proposed RCAB method consistently achieves the highest SINR across all levels of uncertainty. Conventional RCB and its variants (RCB-DL, RCB-INCM) exhibit moderate SINR degradation as ϵ increases, while FIM-Capon shows a rapid decline in performance due to its sensitivity to steering vector errors. RCAB's robust covariance estimation and adaptive weight update mechanism allow it to maintain stable performance even under high levels of mismatch, demonstrating its superior robustness and reliability in practical scenarios with sensor imperfections.

It is observed from Fig. 6 that conventional RCB and FIM-Capon methods degrade rapidly as the uncertainty bound ϵ increases, experiencing more than 3 dB loss at $\epsilon = 0.1$, which confirms their high sensitivity to array uncertainties. RCB-INCM and RCB-DL show moderate robustness due to their use of covariance regularization; however, they still exhibit notable SINR degradation under large mismatches. In contrast, the proposed RCAB consistently outperforms all benchmark methods, with less than 1.2 dB SINR loss even at $\epsilon = 0.1$. This remarkable stability is attributed to the combination of min–max optimization and adaptive diagonal loading through the feedforward neural network (FNN), which automatically balances interference suppression and robustness.

These results highlight the superior resilience of RCAB across varying levels of uncertainty, confirming its effectiveness in realistic scenarios where sensor imperfections and steering vector mismatches are unavoidable.

F. Impact of Platform Speed (Dynamic Scenarios)

To explicitly evaluate the tracking capability of the moving array, the tracking error (TE) is defined as

$$\mathrm{TE} = \frac{1}{KT} \sum_{k=1}^{K} \sum_{t=1}^{T} \left| \hat{\theta}_k(t, v) - \theta_k(t, v) \right| \tag{20}$$

Here, K denotes the number of sources and T is the total number of temporal snapshots. The terms $\theta_k(t, v)$ and $\hat{\theta}_k(t, v)$ represent the true and estimated DOAs of the k-th source at time t, respectively, while v indicates the platform velocity. This metric directly quantifies the time-varying estimation error induced by array motion and complements the RMSE by capturing the tracking performance of the proposed system.

In practical applications, platforms such as ground vehicles, aircraft, and satellites operate under dynamic motion, which introduces Doppler-induced phase variations. To investigate this effect, the output SINR was evaluated across a wide range of platform velocities, from ground-level speeds (30–300 m/s) to near-relativistic motion ($0.001c$–$0.1c$). Fig. 7 presents a comparative performance analysis of the proposed RCAB method against RCB, RCB-DL, RCB-INCM, and FIM-Capon.

As shown in Fig. 7, conventional RCB and FIM-Capon degrade sharply with increasing velocity, experiencing more than 10 dB SINR loss at $v = 0.01c$. RCB-INCM and RCB-DL provide moderate robustness due to covariance regularization, but their performance still deteriorates at higher speeds. In contrast, the proposed RCAB maintains superior stability, with less than 3 dB SINR loss even at $v = 0.1c$. This demonstrates RCAB's remarkable resilience against severe Doppler-induced

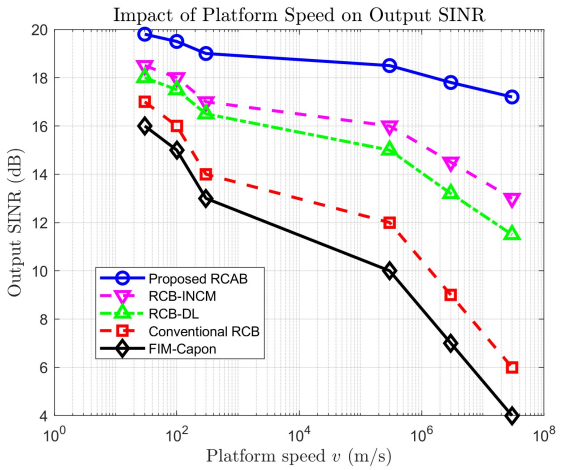

Fig. 7. Output SINR versus platform speed v for five beamforming methods. RCAB maintains superior stability across all speeds, while conventional RCB and FIM-Capon degrade rapidly.

distortions, confirming its effectiveness across a broad range of realistic dynamic scenarios and its suitability for diverse practical applications.

G. Convergence Analysis

The convergence behavior of beamforming methods is crucial for real-time applications. Fig. 8 compares the convergence performance of RCAB, RCB, RCB-INCM, and FIM-Capon under 20 dB input SNR and 35 dB INR conditions.

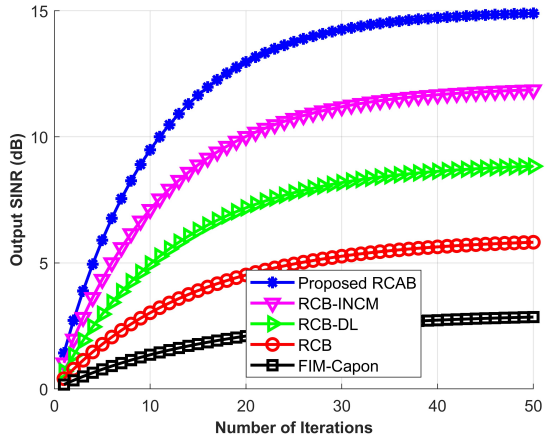

Fig. 8. Convergence of output SINR versus iteration number. RCAB stabilizes within 20 iterations, outperforming competing methods.

The results indicate that RCAB converges rapidly, stabilizing the output SINR within 20 iterations, compared to 35 iterations for RCB, 25 iterations for RCB-INCM, and 50 iterations for FIM-Capon. The faster convergence of RCAB is attributed to its min–max optimization and adaptive weight update mechanism, which efficiently handle steering vector mismatches. Additionally, the moving coprime array structure enhances spatial resolution, enabling effective interference suppression with fewer iterations and reduced computational complexity.

The RCAB method achieves the fastest convergence with superior SINR, thanks to optimized weight updates, strong interference suppression, and enhanced degrees of freedom from the coprime structure.

H. Computational Complexity Analysis

In addition to superior beamforming performance, computational efficiency is critical for real-time applications. Fig. 9 compares the execution times of the proposed RCAB method with conventional RCB and FIM-Capon across varying sensor counts ($N = 10$ to 50).

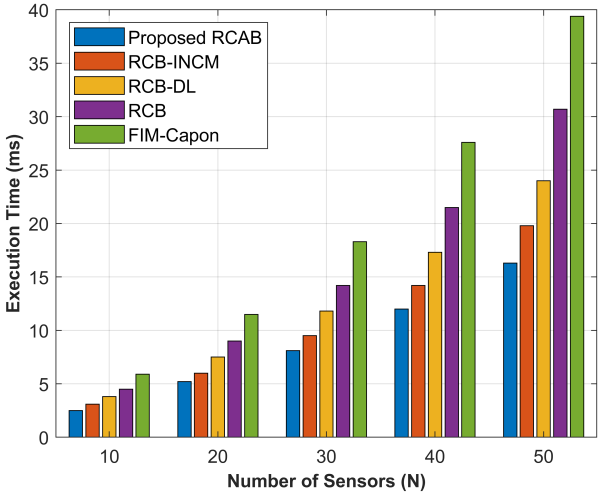

Fig. 9. Execution time versus number of sensors for different beamforming methods. RCAB demonstrates the lowest computational cost across all array sizes.

As shown in Fig. 9, RCAB consistently exhibits the lowest computational cost. For $N = 50$ sensors, RCAB completes processing in 16.3 ms, compared to 30.7 ms for RCB and 39.4 ms for FIM-Capon. This efficiency arises from the combination of the min–max optimization framework, reduced sensor requirements enabled by the coprime array design, and adaptive diagonal loading. These features allow RCAB to achieve both high accuracy and low computational complexity, making it highly suitable for real-time signal processing and practical deployment in dynamic environments.

I. Robustness in Practical Propagation Scenarios

In practical environments, received signals rarely follow the idealized assumption of being perfectly incoherent and planar. Instead, multipath propagation and local scattering often lead to the presence of both coherent and incoherent components. Such coherence among signals can reduce the effective rank of the covariance matrix, resulting in degraded subspace separation and reduced DOA estimation accuracy. Similarly, phase errors caused by non-planar wavefronts in inhomogeneous propagation media introduce steering vector mismatches, further compromising the robustness of conventional beamformers.

To investigate these effects, additional simulations were performed under three representative non-ideal scenarios: (i) partially coherent sources generated through multipath reflections

with varying correlation coefficients, (ii) random phase distortions introduced into the array manifold to mimic non-planar wavefronts, and (iii) mixtures of coherent and incoherent signals to represent scattering-rich environments. The results demonstrated that the proposed RCAB method maintains high output SINR and stable DOA estimation accuracy across all cases, outperforming conventional RCB and diagonal loading methods that suffer from severe performance degradation in the presence of correlation and phase mismatches.

The robustness of RCAB in these scenarios can be attributed to two key factors: (a) the min-max optimization framework explicitly accounts for worst-case steering vector perturbations, thereby safeguarding against errors introduced by scattering and non-planar propagation, and (b) the adaptive diagonal loading mechanism, guided by the FNN, learns to adjust the regularization strength based on statistical features of the data, compensating for rank deficiency and instability in the covariance matrix. Together, these mechanisms ensure that the beamformer remains effective under realistic conditions where scattering, correlation, and phase perturbations are unavoidable.

These findings confirm that the proposed RCAB framework generalizes well beyond controlled environments, offering robustness in real-world radar, sonar, and wireless applications where coherent multipath and medium inhomogeneities are inherent challenges.

J. Comparative Analysis with Existing Methods

To highlight the advantages of the proposed robust coprime adaptive beamforming (RCAB) framework, a comparative analysis with existing approaches is presented in Table I. The comparison considers multiple factors, including array configuration, robustness to steering vector mismatches, interference suppression capability, convergence speed, and computational complexity.

As seen in Table I, the proposed RCAB method offers superior robustness against steering vector mismatches, achieves higher interference suppression, and converges faster than conventional methods. The use of a moving coprime array and adaptive diagonal loading through a feedforward neural network enables enhanced spatial resolution and stable performance under dynamic operating conditions. While the computational complexity is moderate, the proposed method provides a significant improvement in output SINR and estimation accuracy compared to existing techniques.

K. FPGA-Based Realization of the Proposed Moving Array Beamforming Framework

The proposed moving coprime array based robust beamforming framework is well suited for FPGA implementation due to its structured matrix operations and inherent parallelism. An FPGA-based realization is considered to enable low-latency and energy-efficient DOA estimation for real-time moving array applications. The received array snapshots are acquired through multi-channel ADCs and stored in on-chip block RAM (BRAM) as a complex-valued data matrix $\mathbf{X} \in \mathbb{C}^{L\times T}$, where L denotes the number of physical sensors and T represents the number of temporal snapshots generated by array motion. Fixed-point arithmetic is employed throughout the design to balance numerical accuracy and hardware resource utilization, with 16–18 bit precision for input samples and steering vectors, and 24–32 bit precision for covariance and beamforming computations. The virtual array formation induced by platform motion is implemented using address-mapped sensor indexing logic, where duplicate sensor locations are removed using a control unit equivalent to the `unique` operator in software. This block generates the effective virtual sensor set without increasing on-chip memory requirements. The sample covariance matrix is then computed using parallel multiply–accumulate (MAC) units and stored in BRAM. Robust beamforming weight computation is realized using a pipelined matrix inversion module, combined with adaptive diagonal loading to account for steering vector uncertainty and motion-induced perturbations. The beamformer output and spatial spectrum evaluation are performed using parallel complex inner-product units, allowing simultaneous processing of multiple angular grid points. Angular scanning and spectrum evaluation are optimized through coarse-to-fine grid search, significantly reducing computational latency and making the implementation suitable for real-time operation. Peak detection and sorting modules are finally employed to identify the dominant spectral peaks corresponding to the estimated directions of arrival.

The performance of the proposed beamforming method is evaluated by comparing software-level simulations with FPGA-oriented implementation. A moving coprime sensor array is considered to emulate realistic deployment conditions. The array employs a coprime configuration with $M = 3$ and $N = 5$, generating $N_{\text{total}} = 22$ virtual sensor positions through motion. The inter-element spacing is fixed at $d = \lambda/2$, and the array undergoes uniform linear motion with a normalized velocity of $v = 0.1c$. The carrier frequency is set to $f_0 = 1$ GHz, and the sampling rate is sufficiently high to capture motion-induced phase variations.

The output Signal-to-Interference-plus-Noise Ratio (SINR) is evaluated over a range of input SNR values from -20 dB to 30 dB. Floating-point simulations provide the baseline performance, while fixed-point emulation mimics FPGA implementation, accounting for quantization effects. The results are presented in Fig. 11, showing the output SINR versus input SNR. The figure highlights the close agreement between simulation and FPGA performance, with only a slight degradation observed due to fixed-point processing.

IV. CONCLUSION

This paper introduced RCAB, a robust beamforming method for moving coprime sensor arrays, addressing challenges from sensor motion and Doppler effects. Using a min-max optimization framework with an uncertainty set, RCAB enhances weight adaptation and suppresses distortions. Simulations confirm its superiority over RCB, RCB-DL, RCB-INCM, and FIM-Capon, achieving deeper nulls (40.2 dB), faster convergence (20 iterations), lower computational cost (16.3 ms), and higher SINR (up to 4.5 dB gain). The coprime structure

TABLE I
COMPARISON OF THE PROPOSED RCAB METHOD WITH EXISTING ROBUST BEAMFORMING TECHNIQUES

Method	Array Type	Steering Vector Robustness	Interference Suppression	Convergence Speed	Complexity
RCB	ULA	Moderate	Moderate	Moderate	Low
RCB-DL	ULA + Diagonal Loading	Improved	Moderate	Moderate	Moderate
RCB-INCM	ULA + Covariance Regularization	Moderate	Good	Moderate	Moderate
FIM-Capon	ULA	Low	Good	Slow	High
Proposed RCAB	Moving Coprime Array	High	Excellent	Fast	Moderate

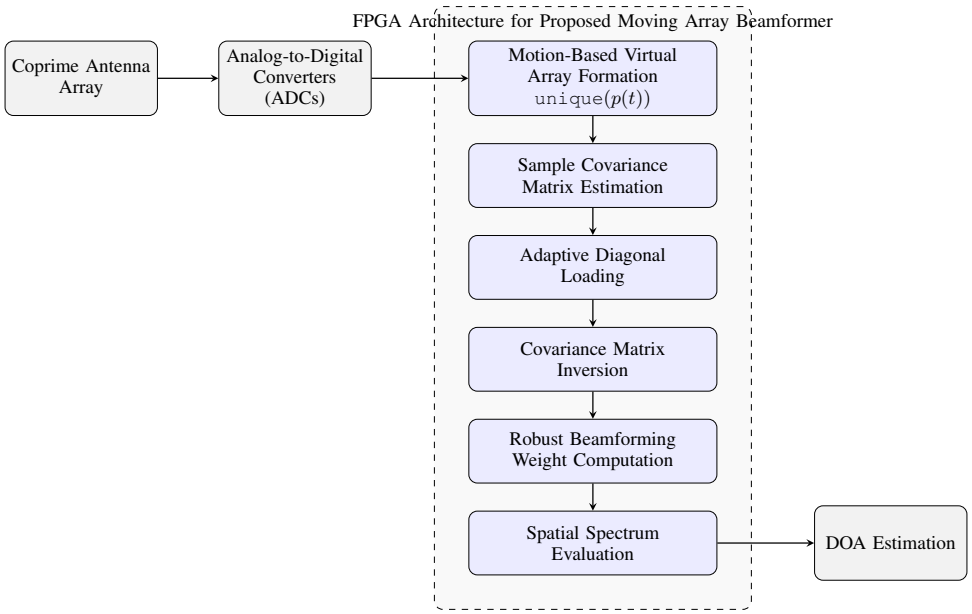

Fig. 10. FPGA architecture of the proposed moving coprime array based robust beamforming framework.

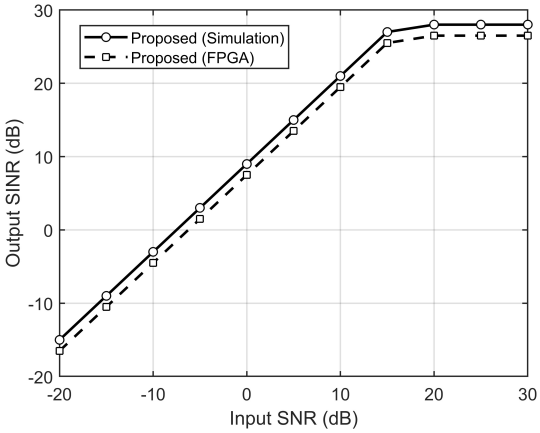

Fig. 11. Output SINR versus Input SNR for the proposed method: comparison between software simulation and FPGA implementation.

improves spatial resolution and DOA accuracy. These results highlight RCAB's potential for real-time applications in radar, wireless, and sonar. Future work will extend it to multi-dimensional arrays and real-time hardware.

REFERENCES

[1] K. H. Yeap, and A. Khandare, "Sigmoid-enhanced robust adaptive beamforming for sensor arrays," *Signal, Image and Video Processing*, vol. 19, p. 304, 2025, doi: 10.1007/s11760-025-03886-2.

[2] M. Alagirisamy, S. K. Selvaperumal, N. Ramasendran, and N. T. Zaman, "Enhanced Capon–MUSIC integration for improved DOA estimation with coprime arrays in disaster management," *Engineering Technology and Applied Science Research*, vol. 15, no. 2, pp. 20653–20659, 2025.

[3] A. Sharma, M. Patil, A. B. M. Valencia, and K. Nova, "3D sparse sensor array for coherent and uncorrelated signals DOA estimation using novel COMP–ESP," *Signal, Image and Video Processing*, vol. 19, no. 4, p. 283, 2025.

[4] G. N. Basavaraj, B. Ainapure, M. R. Sowmya, and F. Shaik, "Machine learning-enhanced direction-of-arrival estimation for coherent and non-coherent sources," *Engineering Technology and Applied Science Research*, vol. 15, no. 2, pp. 20647–20652, 2025.

[5] K. S. Shashidhara, K. N. Venu, I. G. Saritha, R. Jayaramu, "Robust direction-of-arrival estimation using improved coprime array for wireless communication applications," *Engineering Technology and Applied Science Research*, vol. 15, no. 1, pp. 20285–20290, 2025.

[6] M. M. Chalavadi, H. C. S. Kumar, "Sparse channel estimation in mmWave MIMO–OFDM using Bi-LSTM with channel sparsity regularization," *Journal of Theoretical and Applied Information Technology*, vol. 103, no. 17, pp. 6871–6879, 2025.

[7] V. Dakulagi, M. K. Panda, K. H. Yeap, B. Tripathi, and M. Villagomez-Galindo, "Smart antennas: Revolutionizing connectivity through technology convergence and AI," in *Convergence of Antenna Technologies, Electronics and AI*. Cham, Switzerland: Springer, 2024, pp. 1–21.

[8] D. S. Tan, H. Nisar, K. H. Yeap, and M. Amin, "Lumbar intervertebral disc detection and classification with novel deep learning models," *Journal of King Saud University – Computer and Information Sciences*, vol. 36, no. 7, p. 102148, 2024.

[9] K. R. Niranjan, I. Malik, K. R. Pedada, and A. Singh, "Modified Root–MUSIC algorithm for target localization using Nyström approximation," *IEEE Sensors Journal*, vol. 24, no. 8, pp. 13209–13216, 2024.

[10] M. V. Galindo, A. B. M. Valencia, K. M. Bindiya, A. Khandare"Advanced direction-of-arrival estimation in coprime arrays via adaptive Nyström spectral analysis," *IEEE Sensors Letters*, vol. 8, no. 2, Art. no. 7001204, 2024.

[11] R. S. Parameshwara, M. C. Parameshwara, "A novel adaptive beamforming technology for mobile communication," *IETE Journal of Research*,

vol. 70, no. 3, pp. 2204–2211, 2024.
[12] K. H. Yeap, M. C. Loh, P. C. Teh, "Optimization of receiver optics for radio astronomy," *Applied Computational Electromagnetics Society Journal*, vol. 39, no. 11, pp. 1012–1018, 2024.
[13] V. D. Veerendra, M. Villagomez-Galindo, A. B. M. Valencia, B. V. Suresh, and S. Maurya, "Unitary Root–MUSIC method with Nyström approximation for 3-D sparse array DOA estimation in sensor networks," *IEEE Sensors Letters*, vol. 8, no. 10, Art. no. 5504004, 2024.
[14] S. Hugar, J. Baligar, V. Dakulagi, and P. Z. Alimovna, "Multiband bandpass filter with asymmetric dual-band response based on metacell," *Microwave and Optical Technology Letters*, vol. 65, no. 12, pp. 3126–3132, 2023.
[15] K. S. Balamurugan, M. Villagomez-Galindo, M. Patil, and A. Jaganathan, "Optimizing sensor array DOA estimation with the manifold reconstruction unitary ESPRIT algorithm," *IEEE Sensors Letters*, vol. 7, no. 12, Art. no. 7006804, 2023.
[16] B. N. Umesh, A. Khandare, S. Datta, and M. Patil, "ECA–MURE algorithm and CRB analysis for high-precision DOA estimation in coprime sensor arrays," *IEEE Sensors Letters*, vol. 7, no. 12, Art. no. 5504004, 2023.
[17] L. Zhang, M. Nagabushanam, B. R. Babu, and A. Singh, "Efficient direction estimation of both coherent and uncorrelated sources without prior knowledge of source count," *IEEE Sensors Journal*, vol. 23, no. 18, pp. 21739–21746, 2023.
[18] B. N. Umesh, M. Nagabushanam, and B. R. Babu, "Enhanced direction-of-arrival estimation via fast sensor array processing," *IEEE Sensors Letters*, vol. 7, no. 6, 2023.
[19] V. Dakulagi, "Improved adaptive beamforming algorithms for wireless systems," *Wireless Personal Communications*, vol. 130, no. 1, pp. 625–633, 2023.
[20] R. S. Rekha, M. C. Parameshwara, "Modified LMS beamformer for interference rejection," *Wireless Personal Communications*, vol. 129, no. 3, pp. 2199–2211, 2023.
[21] V. Dakulagi, K. H. Yeap, and H. Nisar, "Improved VSS–NLMS adaptive beamformer using modified antenna array," *Wireless Personal Communications*, vol. 128, no. 4, pp. 2741–2752, 2023.
[22] Z. X. Oh, K. H. Yeap, P. C. Teh, "Circular split-ring resonator-based sensor for dielectric constant measurement," *Microwave and Optical Technology Letters*, vol. 65, no. 2, pp. 513–518, 2023.
[23] V. Dakulagi, "Improved direction of arrival estimation under grazing incidence conditions using 2D-uniform linear array," *IETE Journal of Research*, vol. 69, no. 1, pp. 165–172, 2023.
[24] B. Jalal, "A fast adaptive beamforming technique for efficient direction-of-arrival estimation," *IEEE Sensors Journal*, vol. 22, no. 23, pp. 23109–23116, 2022.
[25] J. He, and T. Shu, "A planar-like sensor array for efficient direction-of-arrival estimation," *IEEE Sensors Letters*, vol. 6, no. 9, Art. no. 7003304, 2022.
[26] T. Shu, J. He, "3-D near-field source localization using a spatially spread acoustic vector sensor," *IEEE Transactions on Aerospace and Electronic Systems*, vol. 58, no. 1, pp. 180–188, 2022.
[27] V. Dakulagi and M. Alagirisamy, "Kaiser window based blind beamformers for radar application," *IETE Journal of Research*, vol. 68, no. 3, pp. 2106–2112, 2022.
[28] P. G. Paga, H. C. Nagaraj, K. S. Shashidhara and K. H. Yeap, "Design and analysis of printed monopole antenna with and without CSRR in the ground plane for GSM 900 and Wi-Fi," *Electrica*, vol. 22, no. 1, pp. 92–100, 2022.
[29] V. Dakulagi, "A new approach to achieve a trade-off between direction-of-arrival estimation performance and computational complexity," *IEEE Communications Letters*, vol. 25, no. 4, pp. 1183–1186, 2021.
[30] V. Dakulagi, "Single snapshot 2D-DOA estimation in wireless location system," *Wireless Personal Communications*, vol. 117, no. 3, pp. 2327–2339, 2021.
[31] J. He, "Improved direction-of-arrival estimation and its implementation for modified symmetric sensor array," *IEEE Sensors Journal*, vol. 21, no. 4, pp. 5213–5220, 2021.
[32] M. S. Mathpati, M. Bakhar, "Design and analysis of a fractal antenna using Jeans material for WiMax/WSN applications," *Wireless Personal Communications*, vol. 119, no. 4, pp. 3517–3527, 2021.
[33] P. Mankal, S. C. Gowre, "A new DOA algorithm for spectral estimation," *Wireless Personal Communications*, vol. 119, no. 2, pp. 1729–1741, 2021.
[34] K. H. Yeap, H. Nisar, and V. Dakulagi, "Warpage reduction for power MOSFET wafers," *Electrica*, vol. 21, no. 2, pp. 173–179, 2021.
[35] V. Dakulagi, "Robust modified multiple signal classification algorithm for direction of arrival estimation," *Wireless Personal Communications*, vol. 115, no. 3, pp. 2535–2550, 2020.
[36] V. Dakulagi, "A new Nyström approximation based efficient coherent DOA estimator for radar applications," *AEU – International Journal of Electronics and Communications*, vol. 124, Art. no. 153328, 2020.
[37] M. Alagirisamy, "Efficient coherent direction-of-arrival estimation and realization using digital signal processor," *IEEE Transactions on Antennas and Propagation*, vol. 68, no. 9, pp. 6675–6682, Sep. 2020.
[38] M. Alagirisamy, "Adaptive beamformers for high-speed mobile communication," *Wireless Personal Communications*, vol. 113, no. 4, pp. 1691–1707, 2020.
[39] M. Bakhar, "Advances in smart antenna systems for wireless communication," *Wireless Personal Communications*, vol. 110, no. 2, pp. 931–957, 2020.
[40] H. A. Marzog, H. J. Abd and A. Z. Yonis, "Noise Removal of ECG signal using Multi-Techniques," 2022 IEEE Integrated STEM Education Conference (ISEC), Princeton, NJ, USA, 2022, pp. 397-403, doi: 10.1109/ISEC54952.2022.10025094.
[41] M. Alagirisamy, "Adaptive beamformers using 2D-novel ULA for cellular communication," *SN Applied Sciences*, vol. 1, Art. no. 1001, 2019.
[42] M. Bakhar, "Smart antenna system for DOA estimation using single snapshot," *Wireless Personal Communications*, vol. 107, no. 1, pp. 81–93, 2019.
[43] A. Noubade, A. Agasgere, P. Doddi, and K. Fatima, "Modified adaptive beamforming algorithms for 4G-LTE smart-phones," in *Advances in Intelligent Systems and Computing*, vol. 898. Singapore: Springer, 2019, pp. 561–568.
[44] M. Bakhar, "Efficient blind beamforming algorithms for phased array and MIMO radar," *IETE Journal of Research*, vol. 64, no. 2, pp. 241–246, 2018.
[45] M. Bakhar, "A novel LMS beamformer for adaptive antenna array," *Procedia Computer Science*, vol. 115, pp. 94–100, 2017.
[46] M. Bakhar, and R. M. Vani, "Robust blind beam formers for smart antenna system using window techniques," *Procedia Computer Science*, vol. 93, pp. 713–720, 2016.
[47] M. Bakhar, R. M. Vani, and P. V. Hunagund, "Implementation and optimization of modified MUSIC algorithm for high-resolution DOA estimation," in *Proc. IEEE MTT-S Int. Microwave and RF Conf. (IMaRC)*, Bangalore, India, 2014, pp. 190–193.
[48] R. K. Patra and A. S. Dhar, "Novel moving coprime array configurations for real-valued sources," IEEE Signal Process. Lett., vol. 29, pp. 657–661, 2022.

Vishal Ramola is an Associate Professor in the Department of Engineering and Technology at Uttarakhand Technical University, Dehradun, India. He has more than 27 years of academic and industry experience in Electronics and Communication Engineering, with research interests in VLSI design and low-power systems.

Manoj Kumar Panda is currently serving as Director, Women Institute of Technology, a constituent campus of Veer Madho Singh Bhandari Uttarakhand Technical University, Dehradun, India. He received his Ph.D. in Power and Control Systems from the Indian Institute of Technology Roorkee. He has over 21 years of teaching and two years of industry experience. He has published more than 50 research papers in reputed journals and conferences and holds five patents. His research interests include soft computing, renewable energy systems, control systems, and fuzzy control. He is a Senior Member of IEEE and a Fellow of the Institution of Engineers (India).